



Regular Article

NiO/Ni/TiO₂ nanocables with Schottky/*p-n* heterojunctions and the improved photocatalytic performance in water splitting under visible light

Xiaochen Ren^a, Peng Gao^{a,b,*}, Xianglong Kong^a, Rui Jiang^a, Piaoping Yang^{a,*}, Yujin Chen^{c,*}, Qianqian Chi^b, Benxia Li^{d,*}

^a Key Laboratory of Superlight Materials and Surface Technology, Ministry of Education, College of Materials Science and Chemical Engineering, Harbin Engineering University, Harbin, Heilongjiang 150001, PR China

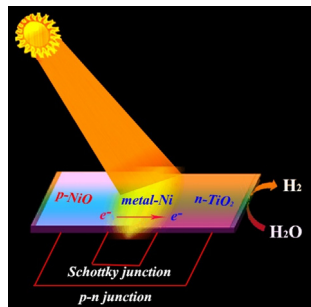
^b College of Material, Chemistry and Chemical Engineering, Hangzhou Normal University, Hangzhou, Zhejiang 310026, PR China

^c College of Science, Harbin Engineering University, Harbin, Heilongjiang 150001, PR China

^d Department of Chemistry, College of Science, Zhejiang Sci-Tech University, Hangzhou 310018, PR China

G R A P H I C A L A B S T R A C T

Sandwich-like heterojunction NiO/Ni/TiO₂ was constructed of cooperative Schottky and *p-n* (SPN) heterojunction by intercalating metal Ni into a NiO/TiO₂ *p-n* junction. It showed a narrowed band, an intensive absorption in visible light region and a higher photocurrent density. And the hydrogen generation rate of the SPN heterojunction under visible light achieved 4653 μmol h⁻¹ g⁻¹.



A R T I C L E I N F O

Article history:

Received 6 May 2018

Revised 19 June 2018

Accepted 23 June 2018

Available online 27 June 2018

Keywords:

TiO₂

Schottky junction

p-n heterojunction

Photocatalytic

Water splitting

A B S T R A C T

Construction of Schottky junction or *p-n* heterojunction is admitted as an effective way for improving the separation of photo-induced carriers through its built-in electric field. In this work, fabrication of cooperative Schottky and *p-n* (SPN) heterojunction has been realized by intercalating metal Ni into a NiO/TiO₂ *p-n* junction, forming a NiO/Ni/TiO₂ Sandwich-like heterojunction. The special heterostructure was confirmed by X-ray powder diffraction (XRD), X-ray photoelectron spectroscopy (XPS), scanning electron microscopy (SEM), transmission electron microscopy (TEM) and the high-resolution transmission electron microscopic (HRTEM), Brunauer Emmett Teller (BET). After a serial of contrast experiments with solo Schottky or *p-n* junction, it was found that the electron-hole separation in this NiO/Ni/TiO₂ SPN heterojunction was enhanced through charge transfer channel, and it was also in accordance with their related optical and photoelectrical properties characterizations, such as photoluminescence (PL) spectrum and UV-Vis diffused reflectance spectra. In the following photocatalytic water splitting process under visible

* Corresponding author at: Key Laboratory of Superlight Materials and Surface Technology, Ministry of Education, College of Materials Science and Chemical Engineering, Harbin Engineering University, Harbin, Heilongjiang 150001, PR China.

E-mail addresses: gaopeng@hrbeu.edu.cn (P. Gao), yangpiaoping@hrbeu.edu.cn (P. Yang), chenyujin@hrbeu.edu.cn (Y. Chen), libx@mail.ustc.edu.cn (B. Li).

light, the hydrogen generation rate of NiO/Ni/TiO₂ reached up to 4653 $\mu\text{mol h}^{-1} \text{g}^{-1}$, which was 10.2, 6.7 and 2.3 times of those of TiO₂ (457 $\mu\text{mol h}^{-1} \text{g}^{-1}$), Ni/TiO₂ (691 $\mu\text{mol h}^{-1} \text{g}^{-1}$) with a Schottky junction and NiO/TiO₂ (2059 $\mu\text{mol h}^{-1} \text{g}^{-1}$) with a *p-n* junction, respectively. This SPN heterojunction with excellent photo-induced electron-hole separation ability opens a new window to exploring photocatalyst for water splitting.

© 2018 Elsevier Inc. All rights reserved.

1. Introduction

As a most simple strategy to obtain hydrogen gas simultaneously without a consumption of other artificial energy, sunlight driven water splitting for H₂ generation depended on semiconductor photocatalyst has marked its debut since 1972 [1]. After several decades' unceasing research, it has arrived at a consensus about the requisite abilities of the semiconductor photocatalyst for water splitting: (I) Possessing a suitable band-gap for visible-light absorption; (II) Booming and transferring more carriers after an incident irradiation; (III) Separating the photo-induced electron and hole efficiently. Points I and II are mainly determined by the semiconductor's intrinsic nature. Dissimilarly, Point III is often artificially tunable. In order to strengthen the separation of photo-induced carriers, *p-n* heterojunction between different semiconductors or Schottky heterojunction formed between carbon layer or metal and conventional semiconductors has been applied by harnessing its built-in electric field [2–5]. However, it has been noticed that some unavoidable drawbacks emerged as using solo *p-n* heterojunction or Schottky heterojunction. For example: In the interface of *p-n* heterojunction, massive accumulated electrons and holes recombined quickly within a very short time and also displayed a low redox ability [6–8]. So the interface between *p* semiconductor and *n* semiconductor activated as a depletion layer and weakened the whole catalytic performance [9]. In the interface of general Schottky heterojunction, there exist much higher contact resistivity ρ_c in the range of $k\Omega\cdot\mu\text{m}$ to $M\Omega\cdot\mu\text{m}$ and longer carrier transfer length L_T [10]. However, under higher backgate-voltage, L_T could be greatly shortened, which further favoring the carrier's transport. Based on the above consideration, here a cooperated heterojunction structure simultaneously containing Schottky heterojunction and *p-n* heterojunction (SPN) is proposed, in which metal layer is intercalated into a *p-n* heterojunction. In this asymmetric structure, through a metal conducting layer a strong built-in electric field of *p-n* heterojunction, the above problems in individual heterojunction have been greatly improved. As a touchstone, in this work NiO/Ni/TiO₂ nanocables have been prepared by a layer-by-layer chemical construction process.

In this NiO/Ni/TiO₂ system, TiO₂ is a classical *n*-type semiconductor photocatalyst (band gap = 3.2 eV for anatase) accompanying with its low cost, high chemical stability, nontoxicity and facile synthesis [11–15]. NiO is a typical *p*-type semiconductor, which shows high photo-induced holes concentration and mobility [16,17]. Also, NiO/TiO₂ with a *p-n* heterojunction has been studied as photocatalyst in the degradation of dyes and organic

compounds [17], water splitting [18] and used in photocathodic protection [19], solar cells [20], etc. There are several methods to synthesize NiO/TiO₂ *p-n* heterojunction. For example: Cui et al. synthesized NiO/TiO₂ hollow microspheres via a hydrothermal route, and the product showed high photoelectrochemical and photocatalytic activities [21]. Shao et al. utilized electroless plating and annealing methods to construct NiO coated TiO₂ nanotube arrays and it exhibited enhanced performance for photocathodic protection of 304 stainless steel [19]. An ultrasonication method was also used by Harraz et al. to prepare mesoporous NiO/TiO₂ nanocomposites and the materials showed high photocatalytic degradation performance to gemifloxacin mesylate and methylene blue [22]. Toupance et al. prepared NiO/TiO₂ heteronanostructures with a sol-gel synthetic route and the product exhibited a photocatalytic activity in H₂ production [23]. A dry mixing route also used to synthesize TiO₂/NiO composite particles by Chou et al. and the power conversion efficiency of the dye-sensitized solar cell based on the product was improved [24]. Other methods, like calcination technology [25] and wetness impregnation [26], were also used to obtain this material. In the previous *p-n* heterojunction photocatalytic works, it was pointed out that its weak conductivity property restricted the excitons' transfer and the following catalytic performance. Recently, reduced graphene oxide was used to form a NiO/rGO/TiO₂ nanostructure, however, the photocatalyst exhibited a low hydrogenation rate (240 $\mu\text{mol h}^{-1} \text{g}^{-1}$) under solar simulator light source [27].

Here, a cooperative Schottky and *p-n* heterojunction named SPN heterojunction has been constructed by intercalating metal Ni into a NiO/TiO₂ *p-n* junction, forming a NiO/Ni/TiO₂ heterostructure. Through their cooperative built-in electric field, the electron-hole separation has been further enhanced compared with solo Schottky or *p-n* junction. At the same time, the SPN heterojunction compound showed a narrowed band, an intensive absorption in visible light region and a higher photocurrent density. And it was found that in the SPN heterojunction the carrier densities was up to $6.27 \times 10^{18} \text{ cm}^{-3}$, higher than that of TiO₂ NTs ($4.99 \times 10^{18} \text{ cm}^{-3}$). The SPN heterojunction's hydrogen generation rate of visible-light driven photocatalytic water splitting (4653 $\mu\text{mol h}^{-1} \text{g}^{-1}$) was about 10.2, 6.7 and 2.3 times of those of TiO₂ (457 $\mu\text{mol h}^{-1} \text{g}^{-1}$), Ni/TiO₂ (691 $\mu\text{mol h}^{-1} \text{g}^{-1}$) with a Schottky junction and NiO/TiO₂ (2059 $\mu\text{mol h}^{-1} \text{g}^{-1}$) with a *p-n* junction, respectively. Simultaneously, to our knowledge, this value was almost the highest in the reported values of related materials, as shown in Table 1. This undoubtedly confirmed the improved electron-hole separation in SPN heterojunction.

Table 1
Photocatalytic performance H₂ generation in some related photocatalysts.

Photocatalyst	Incident light	H ₂ evolution rate ($\mu\text{mol h}^{-1} \text{g}^{-1}$)	Reference
NiO:TiO ₂ composites with type-II band alignment	400 W Hg lamp	1250	[28]
NiO-TiO ₂ defective heterojunctions	300 W Xe lamp	1410	[29]
NiO/TiO ₂ composite nanofibers	300 W Xe lamp	377	[30]
NiO/rGO/TiO ₂ coaxial nanocable	300 W Xe lamp, solar simulator light	240	[27]
TiO ₂ /NiO hybrid shells	350 W Xe lamp, $\lambda > 400 \text{ nm}$	393	[18]
NiO/TiO ₂ /C hybrid shells	350 W Xe lamp, $\lambda > 400 \text{ nm}$	356	[31]
NiO/Ni/TiO ₂ nanocables	300 W Xe lamp, $\lambda > 400 \text{ nm}$	4653	This work

2. Experimental section

2.1. Materials

Titanium powder, Ti (300 mesh, Beijing Mengtai Research Technology Development Center); sodium hydroxide, NaOH (>98%, Tianjin Fengchuan Chemical Reagent Co., Ltd); hydrochloric acid, HCl (35–38%, Tianjin Kemiou Chemical Reagent Co., Ltd); nickel (II) chloride hexahydrate, $\text{NiCl}_2 \cdot 6\text{H}_2\text{O}$ (>98% Tianjin Kemiou Chemical Reagent Co., Ltd), sodium borohydride, NaBH_4 (>98%, Tianjin Kemiou Chemical Reagent Co., Ltd); ethanol, $\text{CH}_3\text{CH}_2\text{OH}$ (>99.7% Tianjin Fuyu Fine Chemical Co., Ltd). All the chemical reagents were of analytical grade and used as received without further purifications. Deionized water was used for all the experiments.

2.2. Preparation of TiO_2 nanotubes (TiO_2 NTs)

TiO_2 NTs were synthesized by an alkaline hydrothermal process. The specific synthetic steps refer to the literature [32].

2.3. Preparation of Ni/TiO_2

The as-prepared TiO_2 NTs (0.5 g) were added into a $\text{NiCl}_2 \cdot 6\text{H}_2\text{O}$ (0.1 M) aqueous solution, and stirred for 2 h under nitrogen atmosphere at room temperature. Then the reaction system was moved to a 0 °C ice-water bath environment. The freshly prepared 0.05 M NaBH_4 (4 equiv of $\text{NiCl}_2 \cdot 6\text{H}_2\text{O}$ to insure the completed reduction) aqueous solution was added dropwise and stirred vigorously at 0 °C for 2 h under nitrogen protection. After that the solution was transferred to centrifuge tube and centrifuged with a speed of 8000 rpm for 10 min each time. In order to remove the superfluous NaBH_4 and other impurities, the collected deposit was washed by distilled water and ethanol for several times. Then, it was dried at 60 °C for 12 h in vacuum oven.

2.4. Preparation of NiO/TiO_2

The synthesis of NiO/TiO_2 at early stage were similar to that of Ni/TiO_2 . After drying, the product was heated at 80 °C for 4 h under oxygen atmosphere.

2.5. Preparation of NiO/Ni/TiO_2

NiO/Ni/TiO_2 were synthesized through a controlled oxidation procedure of Ni/TiO_2 sample. The Ni/TiO_2 sample was exposed to the air for 2 h at room temperature and then stored in a glove box full of Ar gas.

2.6. Determination of physicochemical properties

All the samples in the following measurement were added in a same amount and each of the instrument's parameter settings was consistent.

X-ray powder diffraction (XRD) analysis was carried out with a Japan Rigaku D/max-rA with $\text{Cu K}\alpha$ X-ray tube. The scan rate was $5^\circ \cdot \text{s}^{-1}$ and in the range of 10–80°. The morphology and the elemental analysis of the samples were analyzed by Scanning electron microscopy (SEM) used a SU-70 (Hitachi, Japan) scanning electron microscope with an accelerating voltage of 20 kV. The Transmission electron microscopy (TEM) and the high-resolution transmission electron microscopic (HRTEM) carried out with a JEOL HRTEM (JEM2010 electron microscope) with an accelerating voltage of 200 kV. X-ray photoelectron spectroscopy (XPS) data were obtained by a PHI 5700 ESCA electron spectrometer at Retarding pattern using $\text{Al K}\alpha$ excitation and a hemisphere detector. The

Brunauer Emmett Teller (BET) specific surface area of the samples was analyzed by Micromeritics TriStar 3020 nitrogen adsorption apparatus. All of the prepared samples were preprocessed at 120 °C for 2 h prior to nitrogen adsorption measurement nanotubes. The photoluminescence (PL) spectrum was measured using a spectrophotometer (Jobin Yvon Fluorolog 3-221) with a Xe lamp (450 W) as excitation source at the excitation wavelength of 320 nm. UV-vis diffused reflectance spectra used a UV-vis spectrophotometer (UV2550, Shimadzu, Japan) to obtain the absorbance spectra and BaSO_4 was used as the reference sample, scanning range was 200–800 nm and scanning rate at 200 nm/min. The electrochemical impedance spectroscopy (EIS) experiment, photocurrent density characterizations and Mott-Schottky analysis were performed via electrochemical workstation CHI 660D (Chenhua, China) with three-electrode system in 1 M Na_2SO_4 solution. Pt foil and saturated Ag/AgCl were used as the counter electrode and reference electrode.

2.7. Photocatalytic activity of synthesized materials

The photocatalytic hydrogen production experiments were performed in a top-irradiation quartz flat-bottom container (500 mL) connected with a closed gas circulation system. The circulating water system (LX-300, Beijing, Changliu, China) was set to 5 °C. Firstly 0.1 g catalyst powder was added into a 100 mL aqueous solution of methanol, in which the volume ratio of water: methanol was 4:1. Then three drops of 0.001 M H_2PtCl_6 were added as co-catalyst. A 300 W xenon arc lamp (CEL-HXF300, Beijing, AULTT, China) was used to trigger the photocatalytic reaction and a cutoff filter was employed to achieve visible-light ($\lambda > 400$ nm) irradiation. The amount of H_2 evolution was measured using an on-line gas chromatograph (SP7800, TCD, molecular sieve 0.5 nm, N_2 carrier, Beijing Keruida Limited). The apparent quantum efficiency (QE) of the photocatalysts for hydrogen generation was measured using the same reaction condition with a bandpass filter (420 nm) installed in xenon arc lamp. It was calculated according the following equation:

$$\text{QE}[\%] = \frac{(\text{the number of evolved } \text{H}_2 \text{ molecules}) \times 2}{\text{the number of incident photons}} \times 100\% \quad (1)$$

3. Results and discussion

3.1. Compositions and structures of the products

The crystal structures of the pristine TiO_2 and the as-obtained nanocomposites were firstly characterized by XRD measurements, as shown in Fig. 1a. All samples had the characteristic diffraction peaks at 25.8°, 37.8°, 48.0°, 53.9°, 55.0° and 62.7°, corresponding to (1 0 1), (0 0 4), (2 0 0), (1 0 5), (2 1 1) and (2 0 4) facets of anatase TiO_2 (JCPDS No. 21-1272), respectively. In Ni/TiO_2 sample, the peaks located at 44.5°, 51.8° were attributed to (1 1 1) and (2 0 0) crystal planes of Ni (JCPDS No. 04-0850). The diffraction peaks' strength of Ni in NiO/Ni/TiO_2 were decreasing for the outer NiO formed. And no peak belong to nickel oxide was found in NiO/TiO_2 and NiO/Ni/TiO_2 samples, because the existence of NiO was amorphous and it was also verified by the following characterization. In order to confirm their exact composition, XPS characterizations were then conducted, as shown in Fig. 1b, c and d. C 1s lined at 284.6 eV was used to calibrate the elements' peak positions, such as Ni, Ti, and O elements. It was seen in Fig. 1c that their Ti 2p spectra exhibited two contributions, $2p_{1/2}$ and $2p_{3/2}$ located at 463.9 eV and 458.0 eV, which were assigned to Ti^{4+} in TiO_2 [33]. After decorated by metal Ni, it was seen that the peaks at 852.2 eV and 870.7 eV assigned to Ni $2p_{3/2}$ and Ni $2p_{1/2}$, 858.8 eV and

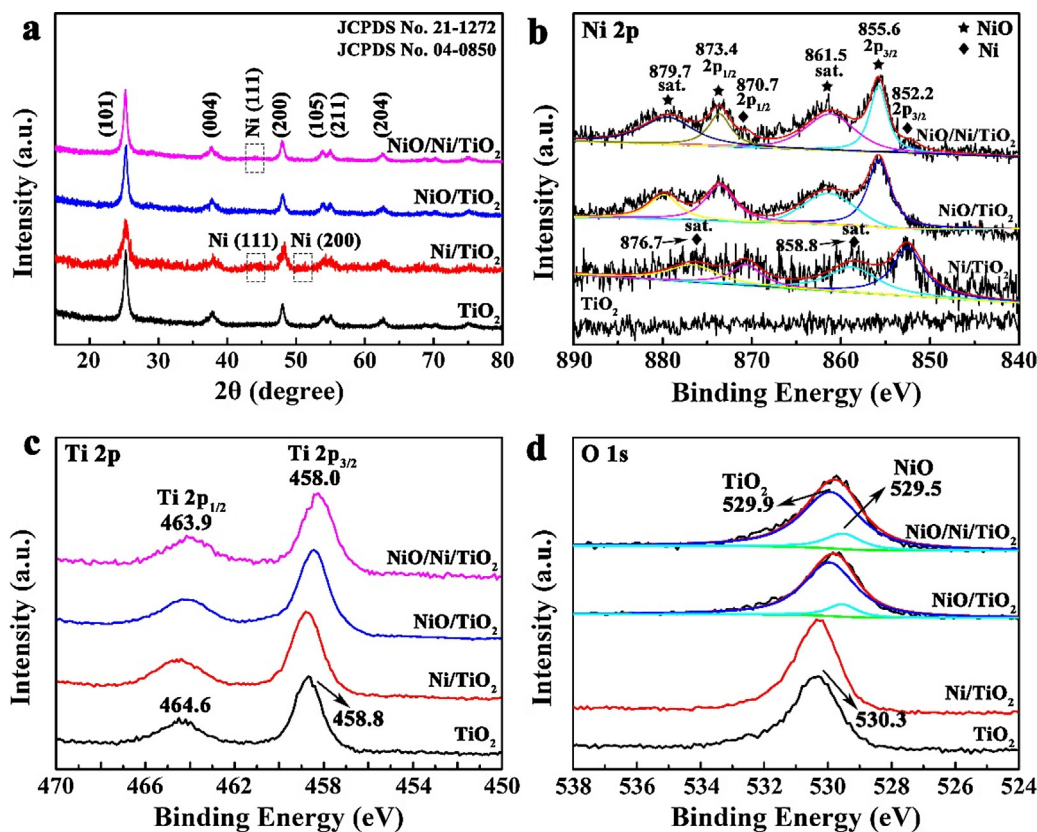


Fig. 1. (a) XRD patterns; XPS spectra of (b) Ni 2p, (c) Ti 2p, (d) O 1s of TiO₂ precursor, Ni/TiO₂, NiO/TiO₂ and NiO/Ni/TiO₂ (8.17% Ni) samples.

876.7 eV of their respective satellite peaks were displayed, as shown in Fig. 1b [34,35]. So Ni/TiO₂ composite was obtained as expected by us. With the oxidation of the above sample, major peaks of Ni 2p_{3/2} (855.6 eV) and Ni 2p_{1/2} (873.4 eV) identical with Ni²⁺ [36] and O 1s peaks of lattice oxygen of NiO [37] were revealed, as shown in Fig. 1d. The corresponding satellite peaks of NiO at 861.5 eV and 879.7 eV were also observed [38]. O 1s of TiO₂ had a little shift to lower binding energy (Fig. 1d), it was because the formed of NiO influenced a space charge layer (band bending) at the interface of nanocomposites, and the phenomenon has also been found in the previous research [23]. As expected by us, NiO/Ni/TiO₂ composites were also obtained, though the signal of NiO wasn't found in its XRD pattern (Fig. 1a). In addition, NiO/Ni/TiO₂ composite with different Ni contents (the molar ratios of Ni to Ti were 1.36%, 2.72%, 5.44%, 8.17% and 10.89% respectively) have also been prepared, as shown in Fig. S1. With the increase of Ni content in the composites, the peaks of Ni became more and more noticeable. So through a serial of controlled experiments, different hetero-structured composites, such as Ni/TiO₂ with Schottky heterojunction, NiO/TiO₂ with *p-n* heterojunction and NiO/Ni/TiO₂ with SPN heterojunction have been successfully prepared.

Supplementary data associated with this article can be found, in the online version, at <https://doi.org/10.1016/j.jcis.2018.06.071>.

The morphologies and microstructures of the samples were further verified by TEM and HRTEM examinations, as shown in Fig. 2. It was seen that all the samples maintained one-dimensional structures and the lattice fringe of TiO₂ NTs displayed interplanar spacing of 3.54 Å, which was well matched with (1 0 1) planes of the crystal anatase TiO₂ [39]. Lattice fringe spacing of 2.03 Å corresponding to (1 1 1) plane of Ni [35] was observed in Ni/TiO₂ and NiO/Ni/TiO₂ (Fig. 2f and l). In addition, no lattice fringe spacing of NiO was found in the corresponding samples. That was agreed

with the XRD results, after the following decoration and oxidation, crystalline metal Ni with exposed (1 1 1) facet and amorphous NiO formed. Also it was provided that the diameter of TiO₂ NTs was about 10.9 nm, Ni/TiO₂ 11.4 nm, NiO/TiO₂ 12.1 nm and NiO/Ni/TiO₂ 12.0 nm on average.

The following scanning electron microscopy (SEM) measurements also demonstrated the above results. As shown in Fig. 3a–d, the diameters of the TiO₂-based nanocables gradually became bigger (from 10.9 nm to 12.1 nm) and the surfaces were changed rougher with the formation of metal Ni and NiO. The element mapping and EDX analysis of the NiO/Ni/TiO₂ nanocables were conducted, as shown in Fig. 3e–i. It was seen that Ni, O and Ti elements were uniformly distributed in the sample. All the above discussed results confirmed that NiO and Ni have been successfully loaded on the outer surfaces of TiO₂ NTs. The changes of their surfaces were further investigated by N₂ adsorption–desorption isotherm measurements. As shown in Fig. S2, the specific surface area of TiO₂ NTs was 95.69 m² g⁻¹, Ni/TiO₂ 120.22 m² g⁻¹, NiO/TiO₂ 147.09 m² g⁻¹ and NiO/Ni/TiO₂ 140.53 m² g⁻¹.

3.2. Optical and photoelectrical properties of the products

Then, the responses to visible-light of the as-prepared samples have also been investigated. Fig. 4a provided typical UV–Vis absorption spectra of the four samples. All the samples represented a sharp absorption at around 380 nm due to TiO₂ and no absorption in the visible light range was found, which was consistent with previous research results [13]. But after decoration, the visible-light absorption was obviously increased (TiO₂ < Ni/TiO₂ < NiO/TiO₂ < NiO/Ni/TiO₂). In Ni/TiO₂, the enhanced absorption after 380 nm due to the electronic transitions of metallic nickel [36]. And in NiO/TiO₂ sample, there was also a strengthened visible light absorption, that is because the NiO loading influenced electronic

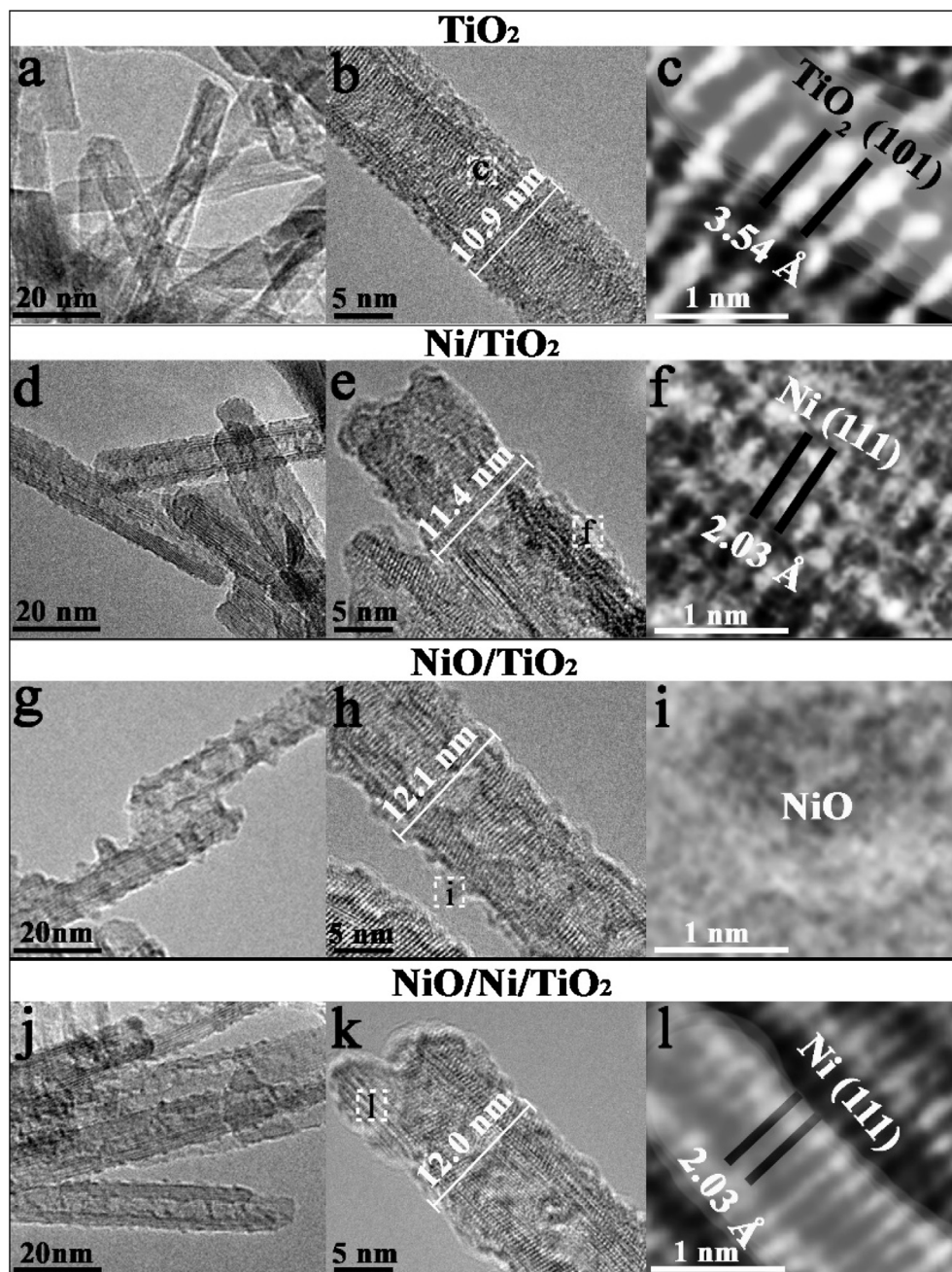


Fig. 2. TEM, HRTEM and partial magnification of HRTEM images of TiO₂ NTs (a)–(c); Ni/TiO₂ (d)–(f); NiO/TiO₂ (g)–(i) and NiO/Ni/TiO₂ (8.17% Ni) (j)–(l).

structure and the vacant 3d states of nickel extended the photo-response in visible region [28,40]. It should be noticed that there was a absorption peak around 450 nm which belonged to the absorption of electron transfer from Ni²⁺ to Ti⁴⁺ [28], so it proved NiO and TiO₂ were connected directly in NiO/TiO₂. NiO/Ni/TiO₂ sample showed the greatest increase, indicated the synergistic effect of the *p-n* junction and Schottky junction. Light absorption is one of the important factors affecting photocatalytic performance. Fig. S3 is the UV–Visible absorption spectra of different Ni content samples. It can be seen that, with the increase of Ni element added, the light absorption showed a growing trend, but it began to decline when Ni content exceed 8.17%. It suggested that the superabundant Ni coating affected the visible-light absorption of the composite, which may due to the formation of thicker NiO layer. This layer affected the visible-light absorption of metal Ni. So the optimal co-catalyst content should be considered in the

synthesis. In addition, the band gaps were decreased from 3.06 eV to 2.57 eV after compositing (Fig. 4b), and it has been reported that the Ti and Ni 3d states could be contributed to decrease the energy gap of TiO₂ thus promoting the visible light absorption [18].

PL spectrum is generally used to evaluate the separation and recombination of photo-generated carriers [41]. As shown in Fig. 4c, a peak around 470 nm belonged to the recombination signal was found with a 320 nm excitation wavelength at room temperature, which showed a similar result compared to the previous work [12]. TiO₂ and NiO/Ni/TiO₂ showed the highest and lowest emission peak intensity respectively, indicating that NiO/Ni/TiO₂ had the lowest recombination rate of electrons and holes compared with other samples [42,43]. At the same time, as shown in Fig. 4d, their Nyquist plots demonstrated that NiO/Ni/TiO₂ had a least arc radius, implying a least resistance and more efficient carrier transportation in the system [44]. Then their photocurrent

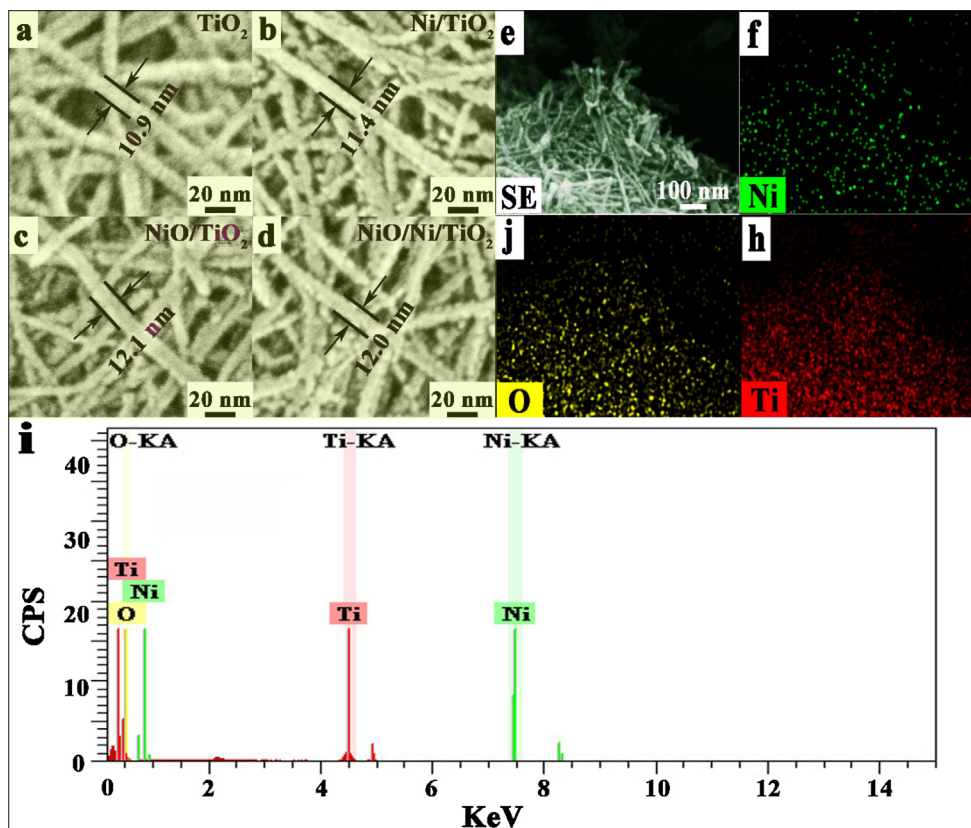


Fig. 3. (a)–(d) SEM images of the TiO_2 , Ni/TiO_2 , NiO/TiO_2 and NiO/Ni/TiO_2 (8.17% Ni) samples; (e)–(h) Element mappings of NiO/Ni/TiO_2 (8.17% Ni) nanocables; (i) EDX spectrum of the NiO/Ni/TiO_2 (8.17% Ni) nanocables.

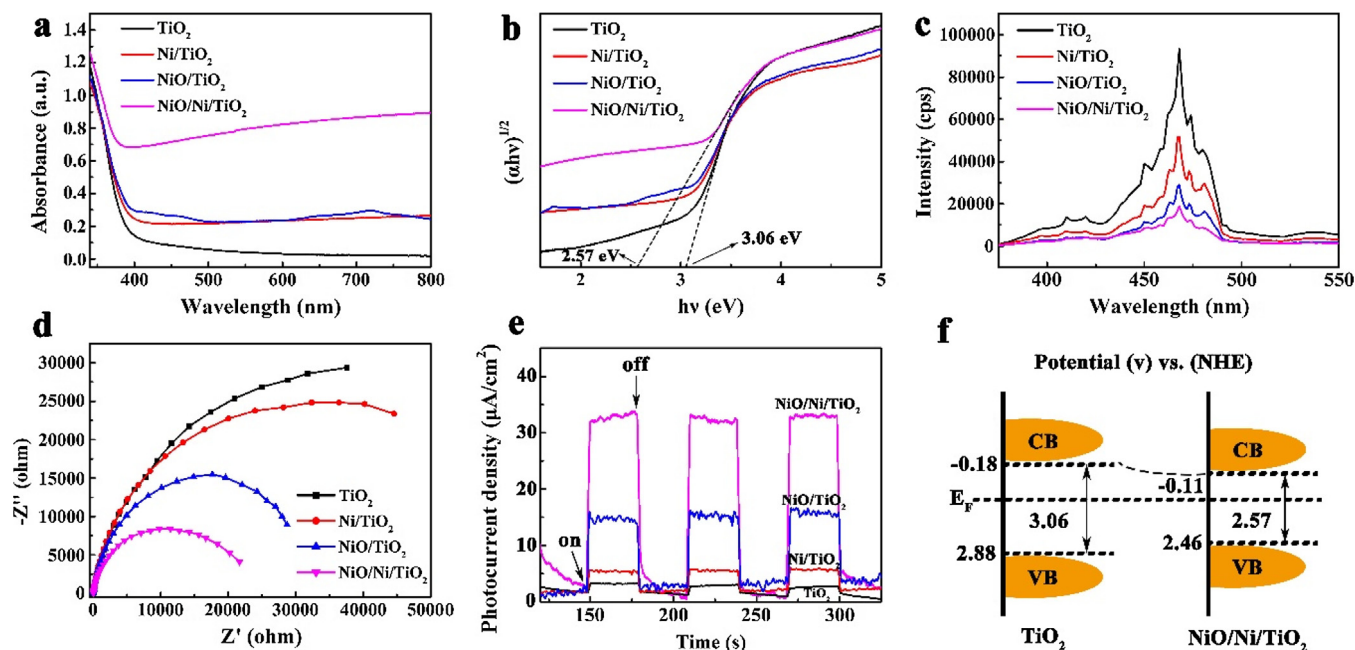


Fig. 4. (a) and (b) UV–Visible absorption spectra and its corresponding Tauc plots; (c) PL emission spectra, (d) EIS Nyquist plots and (e) photocurrent density characterizations by xenon lamp (300 W, $\lambda > 400$ nm) of TiO_2 , Ni/TiO_2 , NiO/TiO_2 and NiO/Ni/TiO_2 (8.17% Ni) samples; (f) The band structures of TiO_2 NTs and the NiO/Ni/TiO_2 (8.17% Ni) nanocables.

densities were tested by a periodic switch (30 s) with a xenon lamp light source (300 W, $\lambda > 400$ nm) on or off, as displayed in Fig. 4d. It was noticed that NiO/Ni/TiO_2 showed the max photocurrent

density ($32.5 \mu\text{A}\cdot\text{cm}^{-2}$), which is about 11.6, 6.1 and 2.1 times of TiO_2 ($2.8 \mu\text{A}\cdot\text{cm}^{-2}$), Ni/TiO_2 ($5.3 \mu\text{A}\cdot\text{cm}^{-2}$) and NiO/TiO_2 ($15.2 \mu\text{A}\cdot\text{cm}^{-2}$). And the energy band structures of TiO_2 NTs and

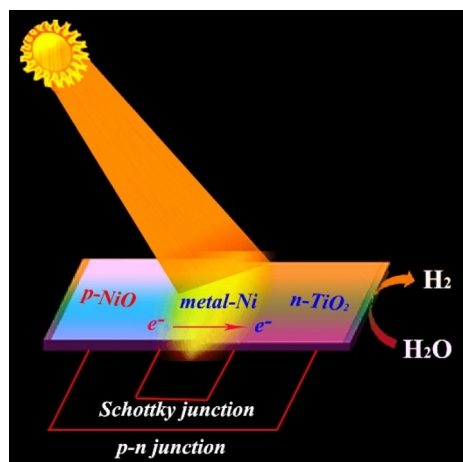
NiO/Ni/TiO₂ nanocables were then measured and calculated. Fig. S4 showed the XPS valence band (VB) spectra of TiO₂ and NiO/Ni/TiO₂. The VBs of TiO₂ and NiO/Ni/TiO₂ were 1.82 eV and 1.36 eV below the Fermi level respectively, implying a 0.46 eV down-shift to a lower binding energy. Their Mott-Schottky plots were used to confirm their Fermi level, which were -0.96 V and -1 V versus normal hydrogen electrode (vs NHE), respectively (Fig. S5). The smaller slope indicated a higher carrier densities and also proved the presence of *p*-type semiconductor NiO. Then the valence band tops of TiO₂ and NiO/Ni/TiO₂ were calculated to be 2.88 eV and 2.46 eV (vs NHE), respectively. From the above VB sites and the band gaps obtained by UV-Vis absorption measurements, the value of conduction band bottoms (vs NHE) were -0.18 eV and -0.11 eV for TiO₂ and NiO/Ni/TiO₂ respectively, as shown in Fig. 4f. Additionally, their carrier densities were calculated from the slope of Mott-Schottky plots using the equation [45,46]:

$$N_d = \frac{2}{e_0 \epsilon \epsilon_0} \frac{d(1/C^2)}{dV} \quad (2)$$

where N_d and C are the carrier density and interfacial capacitance, respectively, e_0 is the electronic charge, ϵ is semiconductor's dielectric constant, ϵ_0 is the permittivity of vacuum, V is the applied voltage. The calculated carrier densities of TiO₂ and NiO/Ni/TiO₂ were $4.99 \times 10^{18} \text{ cm}^{-3}$ and $6.27 \times 10^{18} \text{ cm}^{-3}$, respectively. The calculated carrier densities of TiO₂ and NiO/Ni/TiO₂ were $4.99 \times 10^{18} \text{ cm}^{-3}$ and $6.27 \times 10^{18} \text{ cm}^{-3}$, respectively, which were close values. But the highly improved hydrogenation abilities under visible-light not only because of the more carrier densities in the materials, but also for the real number of remaining active electrons in the fast carrier recombination process. Through our modification, the carrier recombination was decreased and more photo-induced carriers were transmitted to photocatalyst's surface to participate the following critical hydrogen reduction. So the ability of electron-hole transmission and separation in heterojunction was also the critical influencing factors on photocatalysis's performance. All the above results indicated that the NiO/Ni/TiO₂ with a SPN heterojunction should have the best photocatalytic ability under visible-light.

3.3. Photocatalytic properties of the products

The photocatalytic activities in H₂ production of the above samples were measured, as shown in Fig. 5a. NiO/Ni/TiO₂ exhibited a highest photocatalytic activity ($4653 \mu\text{mol h}^{-1} \text{ g}^{-1}$) compared to those of TiO₂ NTs ($457 \mu\text{mol h}^{-1} \text{ g}^{-1}$), Ni/TiO₂ ($691 \mu\text{mol h}^{-1} \text{ g}^{-1}$) and NiO/TiO₂ ($2059 \mu\text{mol h}^{-1} \text{ g}^{-1}$). And the quantum efficiency was up to 8.8% at 420 nm. Meanwhile, as shown in Fig. 5b, the NiO/Ni/TiO₂ with a SPN heterojunction also retained a high photo-



Scheme 1. The schematic diagram of charge separation and electrons' transfer in SPN heterojunction under visible light.

catalytic activity even after five cycles of 25 h reaction, which demonstrated the excellent catalytic stability of this material. In addition, the photocatalytic performances of NiO/Ni/TiO₂ nanocables with different Ni concentrations (the molar ratios of Ni to Ti were 1.36%, 2.72%, 5.44%, 8.17% and 10.89% respectively) have also been conducted, as shown in Fig. S6. It was seen that the NiO/Ni/TiO₂ nanocables with 8.17% Ni exhibited highest hydrogenation rate, which may be due to the effect of different thickness of the NiO/Ni shells.

The mechanism for photocatalytic water splitting process by NiO/Ni/TiO₂ heterostructure is illustrated in Scheme 1. When the light irradiated the sample, the photogenerated electron-hole pairs were created. The Schottky junction and the built-in electric field led a downward flow from NiO to TiO₂. This process effectively refrained the abundant electron-hole from recombining, and provided more active electrons available for the H₂O reduction. The function of Ni here formed Schottky junction and provided a fast electronic transmission channel. A highly charge separation of electron-hole pairs was also realized between NiO and TiO₂, where the inner electric field was established and acted as a potential driving force for movement of the electrons. Finally the excited electrons reduced H⁺ ions to H₂.

4. Conclusion

In summary, NiO/Ni/TiO₂ nanocables with a SPN heterojunction have been successfully synthesized using TiO₂ nanotubes as a template. The characterizations of optical and electrical properties of

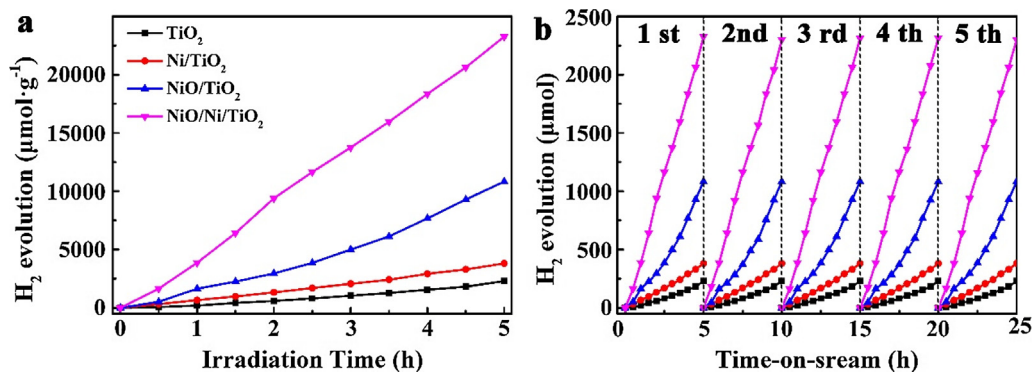


Fig. 5. (a) Photocatalytic activities and (b) Cycling stability in H₂ production of the TiO₂, Ni/TiO₂, NiO/TiO₂ and NiO/Ni/TiO₂ (8.17% Ni) samples.

the system showed outstanding results. As expected by us, an enhanced spatial separation effect of photo-generated electrons and holes has been realized, which resulted in more active performance in the following catalytic reaction. Therefore, the visible-light driven photocatalytic water splitting for H₂ generation based on this SPN heterojunction showed higher rate and good stability. This integration strategy for the spatial separation of electrons and holes based on the construction of two-type heterojunction will greatly promote the application of photocatalytic hydrogen production in practice.

Acknowledgements

We thank the Program for the Pandeng Plan Foundation of Hangzhou Normal University for youth scholars of materials, chemistry and chemical engineering, Natural Science Foundation of Heilongjiang Province (B201603) and Nature Science Foundation of Zhejiang Provincial (LY18E020010) for the financial support of this research.

References

- [1] A. Fujishima, K. Honda, *Nature* 238 (1972) 37–38.
- [2] Z. Zhang, C. Shao, X. Li, C. Wang, M. Zhang, Y. Liu, *A.C.S. Appl. Mater. Interfaces* 2 (2010) 2915–2923.
- [3] Y. Ku, C.-N. Lin, W.-M. Hou, *J. Mol. Catal. A: Chem.* 349 (2011) 20–27.
- [4] L. Gomathi Devi, R. Kavitha, *Appl. Surf. Sci.* 360 (2016) 601–622.
- [5] L. Shang, B. Tong, H. Yu, G.I.N. Waterhouse, C. Zhou, Y. Zhao, M. Tahir, L.-Z. Wu, C.-H. Tung, T. Zhang, *Adv. Energy Mater.* 6 (2016) 1501241.
- [6] S. Bai, J. Jiang, Q. Zhang, Y. Xiong, *Chem. Soc. Rev.* 44 (2015) 2893–2939.
- [7] T. Li, W. Zeng, Z. Wang, *Sens. Actuators B: Chem.* 221 (2015) 1570–1585.
- [8] W. Yin, L. Bai, Y. Zhu, S. Zhong, L. Zhao, Z. Li, S. Bai, *A.C.S. Appl. Mater. Interfaces* 8 (2016) 23133–23142.
- [9] D. Zhang, C. Liu, R. Xu, B. Yin, Y. Chen, X. Zhang, F. Gao, S. Ruan, *Nanotechnology* 28 (2017) 365505.
- [10] H. Liu, M. Si, D. Yexin, A.T. Neal, Y. Du, S. Najmaei, P.M. Ajayan, J. Lou, P.D. Ye, *ACS Nano* 8 (2013) 1031–1038.
- [11] Q. Guo, C. Zhou, Z. Ma, Z. Ren, H. Fan, X. Yang, *Chem. Soc. Rev.* 45 (2016) 3701–3730.
- [12] Y. Yang, P. Gao, Y. Wang, L. Sha, X. Ren, J. Zhang, P. Yang, T. Wu, Y. Chen, X. Li, *J. Mater. Chem. A* 5 (2017) 9198–9203.
- [13] S. Sun, J. Zhang, P. Gao, Y. Wang, X. Li, T. Wu, Y. Wang, Y. Chen, P. Yang, *Appl. Catal. B* 206 (2017) 168–174.
- [14] S. Sun, P. Gao, Y. Yang, P. Yang, Y. Chen, Y. Wang, *A.C.S. Appl. Mater. Interfaces* 8 (2016) 18126–18131.
- [15] B. Li, Y. Hao, B. Zhang, X. Shao, L. Hu, *Appl. Catal. A* 531 (2017) 1–12.
- [16] F. Hashemzadeh, A. Gaffarinejad, R. Rahimi, *J. Hazard. Mater.* 286 (2015) 64–74.
- [17] R. Vinoth, P. Karthik, K. Devan, B. Neppolian, M. Ashokkumar, *Ultrason Sonochem.* 35 (2017) 655–663.
- [18] M. Wang, Y. Hu, J. Han, R. Guo, H. Xiong, Y. Yin, *J. Mater. Chem. A* 3 (2015) 20727–20735.
- [19] C. Han, Q. Shao, J. Lei, Y. Zhu, S. Ge, *J. Alloys Compd.* 703 (2017) 530–537.
- [20] K. Nakamura, T. Oshikiri, K. Ueno, Y. Wang, Y. Kamata, Y. Kotake, H. Misawa, *J. Phys. Chem. Lett.* 7 (2016) 1004–1009.
- [21] J. Li, H. Cui, X. Song, N. Wei, J. Tian, *Appl. Surf. Sci.* 396 (2017) 1539–1545.
- [22] M. Faisal, F.A. Harraz, A.A. Ismail, A.M. El-Toni, S.A. Al-Sayari, A. Al-Hajry, M.S. Al-Assiri, *Ceram. Int.* 44 (2018) 7047–7056.
- [23] M.T. Uddin, Y. Nicolas, C. Olivier, W. Jaegermann, N. Rockstroh, H. Junge, T. Toupance, *PCCP* 19 (2017) 19279–19288.
- [24] C.-S. Chou, Y.-J. Lin, R.-Y. Yang, K.-H. Liu, *Adv. Powder Technol.* 22 (2011) 31–42.
- [25] C. Shifu, Z. Sujuan, L. Wei, Z. Wei, *J. Hazard. Mater.* 155 (2008) 320–326.
- [26] C.-J. Chen, C.-H. Liao, K.-C. Hsu, Y.-T. Wu, J.C.S. Wu, *Catal. Commun.* 12 (2011) 1307–1310.
- [27] X. Yu, J. Zhang, Z. Zhao, W. Guo, J. Qiu, X. Mou, A. Li, J.P. Claverie, H. Liu, *Nano Energy* 16 (2015) 207–217.
- [28] S.A. Rawool, M.R. Pai, A.M. Banerjee, A. Arya, R.S. Ningthoujam, R. Tewari, R. Rao, B. Chalke, P. Ayyub, A.K. Tripathi, S.R. Bharadwaj, *Appl. Catal. B* 221 (2018) 443–458.
- [29] X. Weng, Y. Zhang, F. Bi, F. Dong, Z. Wu, J.A. Darr, *J. Mater. Chem. A* 5 (2017) 23766–23775.
- [30] L. Li, B. Cheng, Y. Wang, J. Yu, *J. Colloid Interface Sci.* 449 (2015) 115–121.
- [31] M. Wang, J. Han, Y. Hu, R. Guo, Y. Yin, *A.C.S. Appl. Mater. Interfaces* 8 (2016) 29511–29521.
- [32] W. Liu, P. Gao, D. Bao, G. Zhang, Y. Chen, G. Chen, Y. Wang, L. Wang, S. Yang, G. Li, Y. Sun, *RSC Adv.* 3 (2013) 6531–6537.
- [33] Y. Yang, P. Gao, Y. Wang, L. Sha, X. Ren, J. Zhang, Y. Chen, T. Wu, P. Yang, X. Li, *Nano Energy* 33 (2017) 29–36.
- [34] V. Mohan, C. Raghavendra, C.V. Pramod, B.D. Raju, K.S. Rama Rao, *RSC Adv.* 4 (2014) 9660–9668.
- [35] L. Sha, P. Gao, T. Wu, Y. Chen, *A.C.S. Appl. Mater. Interfaces* 22 (2017) 40412–40419.
- [36] W.-T. Chen, A. Chan, D. Sun-Waterhouse, T. Moriga, H. Idriss, G.I.N. Waterhouse, *J. Catal.* 326 (2015) 43–53.
- [37] T.V. Thi, A.K. Rai, J. Gim, J. Kim, *J. Power Sources* 292 (2015) 23–30.
- [38] M.A. Peck, M.A. Langell, *Chem. Mater.* 24 (2012) 4483–4490.
- [39] M. Kong, Y. Li, X. Chen, T. Tian, P. Fang, F. Zheng, X. Zhao, *J. Am. Chem. Soc.* 133 (2011) 16414–16417.
- [40] J. Liu, Q. Jia, J. Long, X. Wang, Z. Gao, Q. Gu, *Appl. Catal. B* 222 (2018) 35–43.
- [41] B. Sun, G. Zhou, T. Gao, H. Zhang, H. Yu, *Appl. Surf. Sci.* 364 (2016) 322–331.
- [42] L. Jing, Z.-Y. Yang, Y.-F. Zhao, Y.-X. Zhang, X. Guo, Y.-M. Yan, K.-N. Sun, *J. Mater. Chem. A* 2 (2014) 1068–1075.
- [43] X.-J. Lv, S.-X. Zhou, C. Zhang, H.-X. Chang, Y. Chen, W.-F. Fu, *J. Mater. Chem.* 22 (2012) 18542–18549.
- [44] R. Vinoth, P. Karthik, C. Muthamizhchelvan, B. Neppolian, M. Ashokkumar, *PCCP* 18 (2016) 5179–5191.
- [45] Y. Yang, P. Gao, X. Ren, L. Sha, P. Yang, J. Zhang, Y. Chen, L. Yang, *Appl. Catal. B* 218 (2017) 751–757.
- [46] Z. Wang, C. Yang, T. Lin, H. Yin, P. Chen, D. Wan, F. Xu, F. Huang, J. Lin, X. Xie, M. Jiang, *Energy Environ. Sci.* 6 (2013) 3007–3014.